

Integrability technique for fluid flow induced deformation of a boundary hairJonas Smucker^{1,*}, Zerrin M. Vural^{1,†}, José R. Alvarado^{1,‡}, and Philip J. Morrison^{2,§}¹*Department of Physics and Center for Nonlinear Dynamics, The University of Texas at Austin, Austin, Texas 78712, USA*²*Department of Physics and Institute for Fusion Studies, The University of Texas at Austin, Austin, Texas 78712, USA*

(Received 30 March 2022; accepted 14 July 2022; published 12 August 2022)

The deformation of a dense carpet of hair due to Stokes flow in a channel can be described by a nonlinear integrodifferential equation for the shape of a single hair, which possesses several solutions for a given choice of parameters. Although it was posed in a previous study and it bears a resemblance to the pendulum problem from mechanics, this equation has not been analytically solved until now. Despite the presence on an integral with a nonlinear functional dependence on the dependent variable, the system is integrable. We compare the analytically obtained solution to a finite-difference numerical approach, identify the physically realizable solution branch, and briefly study the solution structure through a conserved energylike quantity. Time-dependent fluid-structure interactions are a rich and complex subject to investigate, and we argue that the solution discussed herein can be used as a basis for understanding these systems.

DOI: [10.1103/PhysRevFluids.7.084001](https://doi.org/10.1103/PhysRevFluids.7.084001)**I. INTRODUCTION**

Beds of hairlike structures interacting with fluids are prevalent in organisms on both micro and macro lengthscales. Their ubiquity in complex and simple organisms is an indication of their versatility. Indeed, there is great diversity in the functionality at either of these lengthscales.

For example, geckos utilize hairlike setae on their feet to promote adhesion to surfaces [1], cricket filiform hairs play a mechanosensitive role [2], and the papillae on hummingbird tongues are used as a “nectar mop” [3]. They serve important roles in nutrient absorption [4,5], surface protection and flow control [6–9], surface adhesion [1,10–12], and fluid entrainment [3,13,14]. They function as mechanosensors, detecting fluid flows [2,7,15–19], predators [20,21], and electric fields [22].

With the improvement of existing manufacturing techniques and the creation of new protocols [23–29], studies have investigated a diverse assortment of systems involving artificial hairs. For example, recent studies have investigated the design potential of hair beds: Hairs placed in a microfluidic channel have been shown to function as pumps [27,30,31], rectifiers [32,33], and micromixers [34–36] making them a design consideration in laboratory-on-chip devices.

Earlier work [32] used the theory of Kirchoff rods to describe the bending of hairs in a channel when subject to shear flow. These authors assumed that the hairs possess linear, isotropic material properties, but undergo finite displacements. The latter consideration makes the problem nonlinear [37], and as a result, in Ref. [32] the problem was solved numerically.

*jsmucker@chaos.utexas.edu

†Present address: Department of Mathematics, UCLA, Los Angeles, CA 90095, USA.

‡alv@chaos.utexas.edu

§morrison@physics.utexas.edu

While there are many numerical methods to deal with such nonlinearities, numerical approaches will only go so far. Biological-scale simulation of hair-beds has yet to be achieved efficiently [38]. There are several reasons for this. Such systems involve many hairs [33] that are free to respond to the ambient fluid flows generated by both external forcing and their neighbors. Additionally, consideration of the hair's inertia makes the governing system of equations stiff [37]. Despite this, large-scale simulation of hairs has been achieved in the graphics community by application of an assortment of optimization techniques [39,40]. However, these techniques have the tradeoff of realism [41].

To further understand these systems, we focus on and solve just the time-independent problem posed in [32] for the profiles of a cantilevered hair-bed subject to shear flow through a channel. We investigate both physical and nonphysical classes of solutions and how to consistently single out the former from the latter.

The paper is organized as follows. In Sec. II, we introduce the basic model and examine how our problem differs from previous studies. We see that the problem arises naturally as a boundary value problem, for which a method for analytical solution is described and implemented in Sec. III. Next, we examine the phase space and discuss how a self-consistency condition associated with the problem influences the solution-structure in Sec. IV. It is here that we also consider the case of angled hairs. We discuss common numerical approaches to solving this class of problem in Sec. V, comparing one such implementation to our solution. We conclude our work with a summary in Sec. VI.

II. PROBLEM FORMULATION

We consider the problem of a cantilevered hair, attached at a flat horizontal boundary, subject to Stokes flow. In this formulation, the hair is represented as a plane curve in Cartesian coordinates with $\mathbf{R} = x(s)\hat{x} + z(s)\hat{z}$, where \hat{x} and \hat{z} are unit vectors. The unit tangent is given by $\hat{\mathbf{T}} = \sin \theta(s)\hat{x} + \cos \theta(s)\hat{z}$, so that $\hat{\mathbf{T}} \cdot \hat{z} = \cos \theta$, and with this parametrization the curvature is given by $d\theta/ds$. The quantity $h(s) = \int_0^s \cos \theta(s') ds'$ represents the height of the hair at position s , with $h(L)$ being the total height.

Let us next focus on the configuration of a hair obtained from moment balance in equilibrium. For an infinitesimal cylindrical section of the hair, this balance yields

$$\mathbf{M}(s + ds) - \mathbf{M}(s) + d\mathbf{r} \times \mathbf{F}_{\text{int}}(s) = 0, \quad (1)$$

where $\mathbf{M}(s) = EI\theta'(s)\hat{y}$ is the bending moment, $d\mathbf{r} = ds\hat{\mathbf{T}}(s)$, and $\mathbf{F}_{\text{int}}(s)$ is the net internal force on the rod segment. For the purpose of this model, the hairs are packed sufficiently dense such that the internal force is derived solely from the fluidic shear stress at the hair-tip.

By assuming Stokes flow with a no-slip boundary condition at the hair-tips, the shear stress is found to be $\frac{\eta v}{H-h(L)}\hat{\mathbf{x}}$, where H , η , and v are the channel height, viscosity, and boundary velocity, respectively. An illustration of the system is shown in Fig. 1, with all relevant parameters presented in Table I. The internal force is this stress times an area:

$$\mathbf{F}_{\text{int}} = \frac{\pi a^2}{\phi} \frac{\eta v}{H - h(L)} \hat{\mathbf{x}}.$$

The first term, $\frac{\pi a^2}{\phi}$, is a characteristic control area covering both the hair-tip and the neighboring fluid. Next, the stress exerted on the hair by the fluid depends on the hair height, or more specifically, the clearance length between the hair-tip and upper channel wall, which is the reason for the denominator $H - h(L)$: a vertical hair would be impacted by a maximum force, while the force is diminished as it entrains in the horizontal direction. A most interesting feature of this formulation is that the relaxed state that results is self-referential because of this denominator; i.e., the solution depends on itself and, as we will see, this gives rise to a self-consistency condition.

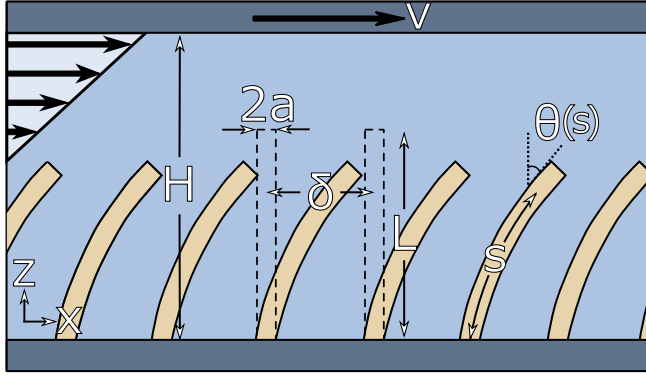


FIG. 1. Illustration of how the fluid-hair system is modeled. Dashed and solid profiles show hairs in an undeformed and a deformed configuration, respectively. The model assumes the fluid velocity becomes zero at the hair-tip, exerting a shear stress $\frac{\eta v}{H-h(L)}$ on the hair.

From Eq. (1) and the definition of \mathbf{M} , we “divide” by ds to obtain

$$EI \frac{d^2\theta(s)}{ds^2} = -\frac{\pi a^2}{\phi} \frac{\eta v \cos \theta(s)}{H - \int_0^L \cos \theta(s') ds'}, \quad (2)$$

which is the equation that will be solved in the course of this paper. We refer the reader to [32,37] for further details regarding its derivation.

Equation (2) can be transformed into the compact nondimensional form

$$\frac{d^2\hat{\theta}}{d\sigma^2} = -\omega_\epsilon^2 \cos \hat{\theta} \quad (3)$$

by introducing

$$\hat{\theta}(\sigma) = \theta(s), \quad \sigma = \frac{s}{L}, \quad \epsilon = \frac{L}{H}, \quad \text{and} \quad \omega^2 = \frac{\pi a^2 L^2 \eta v}{EI H \phi}, \quad (4)$$

and

$$\omega_\epsilon^2 = \frac{\omega^2}{1 - \epsilon \int_0^1 \cos \hat{\theta}(\sigma) d\sigma}. \quad (5)$$

TABLE I. Important system parameters and their associated units.

H	Channel height [L]
L	Hair length [L]
a	Hair radius [L]
ϕ	Packing fraction
δ	Hair-hair centerline spacing [L]
E	Elastic modulus $[M][T]^{-2}[L]^{-1}$
I	2nd area moment of hair's cross-section $[L]^4$
η	Dynamic viscosity $[M][L]^{-1}[T]^{-1}$
v	Imposed fluid velocity $[L][T]^{-1}$
θ	Angle between the local tangent and the vertical
s	Arc length measured from the base of the hair [L]

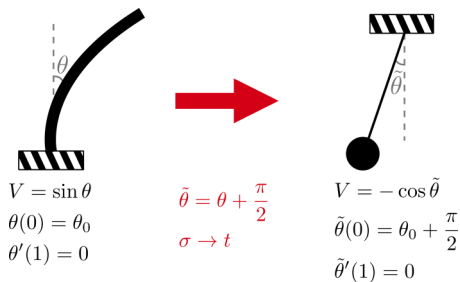


FIG. 2. The hair boundary value problem is mathematically equivalent to that of a pendulum if θ is shifted by $\pi/2$ and $\sigma \rightarrow t$.

The natural boundary conditions for (3) are the following:

$$\hat{\theta}(0) = \hat{\theta}_0 \quad \text{and} \quad \left. \frac{d\hat{\theta}}{d\sigma} \right|_{\sigma=1} = \hat{\theta}'_1 = 0, \quad (6)$$

where $\hat{\theta}_0$ is the angle of attachment of the hair, and $\hat{\theta}'_1 = 0$ means that the hair at its tip has zero curvature. The latter condition can be obtained from the moment balance in Eq. (1). At the end of the hair, there is no upstream ($s > L$) contribution to the balance, implying that $\hat{\mathbf{M}}(1) \equiv EI\hat{\theta}'_1\hat{\mathbf{y}}$ is infinitesimally small. With these definitions, we see that our system has only two dimensionless parameters, ϵ and ω , in addition to the choice of $\hat{\theta}_0$. We will drop the “hats” moving forward to avoid clutter.

This system differs in some ways from the standard pendulum problem of mechanics. For example, we have the trivial difference that there is a shift in the definition of the angle—instead of having $\sin \theta$ on the right-hand side of (3), we have $\cos \theta$. However, there are two essential differences: first, instead of the usual initial value problem, in light of (6), we have a boundary value problem; and second, the system has the self-referential feature mentioned above, i.e., in order to know the effective frequency ω_ϵ of (5) one must first obtain the entire “orbit” $\theta(\sigma)$ to get a self-consistent solution. Although these differences complicate the problem significantly, we will see that the problem remains integrable. We will see that the self-consistency condition together with the boundary value nature of the problem lead to a sort of quantization and a further reduction of parameters.

A “potential” for (3) can be obtained by setting $d^2\theta/d\sigma^2 = -dV/d\theta$, where $V(\theta) = \omega_\epsilon^2 \sin \theta$. The Hamiltonian of this system, which we will call \mathcal{E} , takes the form

$$\mathcal{E} = \frac{1}{2} \left(\frac{d\theta}{d\sigma} \right)^2 + \omega_\epsilon^2 \sin \theta. \quad (7)$$

Because ω_ϵ does not depend explicitly on σ , the timelike variable, conservation of energy, $d\mathcal{E}/d\sigma = 0$, follows immediately. Observe that the curvature, $d\theta/d\sigma$, determines a quantity analogous to the pendulum kinetic energy for this system.

As noted above and indicated in Fig. 2, the potential in the pendulum problem is $-\cos \theta$ and the pendulum oscillates about $\theta = 0$. However, the boundary value problem for the hair is different because the pendulum potential $-\cos \theta$ is shifted by $\pi/2$ from the hair’s potential, $\sin \theta$. Thus, the hair problem is analogous to a pendulum starting at $\theta = \theta_0$, a distance up the potential well, that is then projected further up the well with an initial velocity that is enough for it to hit its turning point at $d\theta/d\sigma = 0$. Therefore, the goal is to determine the initial value of $d\theta/d\sigma$ corresponding to a time (length) for this to occur. To transform our problem to the pendulum problem, we will shift θ by $\pi/2$, i.e.,

$$\bar{\theta} = \theta + \frac{\pi}{2} \quad \Rightarrow \quad \sin(\theta) = -\cos(\bar{\theta}), \quad (8)$$

and therefore

$$\mathcal{E} = \frac{1}{2} \left(\frac{d\bar{\theta}}{d\sigma} \right)^2 - \omega_\epsilon^2 \cos \bar{\theta}. \quad (9)$$

This angle shift is convenient because it allows us to write the solution in the standard form for the pendulum in terms of elliptic integrals, which is a first step toward showing integrability.

III. SOLUTION INTEGRABILITY

Given the formulation of Sec. II, we may begin by following the elementary procedure for reducing the pendulum to quadrature. Using the double-angle formula, $\cos \theta = 1 - 2 \sin^2(\theta/2)$, solving (9) for $d\bar{\theta}/d\sigma$, and integrating gives

$$\pm \frac{\omega_\epsilon}{k} \sigma = \int_{\theta_0/2+\pi/4}^{\theta(\sigma)/2+\pi/4} \frac{d\chi}{\sqrt{1 - k^2 \sin^2 \chi}}, \quad (10)$$

where $\chi = \theta/2$ and

$$k^2 = \frac{2\omega_\epsilon^2}{\mathcal{E} + \omega_\epsilon^2}. \quad (11)$$

The choice in sign in (10) determines whether θ'_0 is positive or negative. While we are primarily interested in hairs with positive base-curvature (corresponding to the positive sign), we include both possibilities for completeness. This quadrature, analogous to that of the pendulum, is the first step toward obtaining integrability of our hair problem.

Before proceeding, there is one issue that must be checked, viz. that $\sqrt{1 - k^2 \sin^2 \chi}$ does not become imaginary; that is, we want to check that $k^2 \sin^2 \chi < 1$ for χ within the limits of integration, and that this is maintained as the upper limit of the integral of (10) extends all the way to $\theta(1)$, which we will denote by θ_1 . For the most part, we expect physical solutions to have

$$0 \leq \theta_1 \leq \pi/2, \quad (12)$$

which we can verify after the solution is obtained, so that according to (7), $\mathcal{E} > 0$. Thus, upon writing $\xi = \mathcal{E}/\omega_\epsilon^2$, (11) becomes $k^2 = 2/(1 + \xi)$ with $\xi \geq 0$. Consequently,

$$1 \leq k^2 \leq 2, \quad (13)$$

and this by itself is insufficient to guarantee $k^2 \sin^2 \chi < 1$. However, because of the second boundary condition of (6) and conservation of the energy of (9),

$$\xi = \sin \theta_1 \quad \Rightarrow \quad 0 \leq \xi \leq 1. \quad (14)$$

Next, using (12) and the fact that $\sin^2 \chi$ achieves its maximum when $\theta = \theta_1$, we obtain

$$\sin^2(\theta_1/2 + \pi/4) = (1 + \sin \theta_1)/2, \quad (15)$$

which follows from elementary trigonometry identities. Therefore with (14), we have

$$k^2 \sin \chi \leq \frac{2}{1 + \xi} \frac{1}{2} (1 + \sin \theta_1) = \frac{1}{1 + \xi} (1 + \xi) = 1. \quad (16)$$

Thus the quadrature integral of (10) is well behaved even with $k^2 > 1$, which is consistent with what we would physically expect.

Proceeding, we can invert and obtain the explicit solution by writing the integral of (10) in terms of elliptic integrals. First, we split the integral as follows:

$$\pm \frac{\omega_\epsilon}{k} \sigma = \int_0^{\theta(\sigma)/2+\pi/4} \frac{d\chi}{\sqrt{1 - k^2 \sin^2 \chi}} - \int_0^{\theta_0/2+\pi/4} \frac{d\chi}{\sqrt{1 - k^2 \sin^2 \chi}}, \quad (17)$$

and notice that the second integral of (17) is an incomplete elliptic integral of the first kind, which we move to the left-hand side, yielding

$$\pm \frac{\omega_\epsilon}{k} \sigma + \mathbf{F}\left(\frac{\theta_0}{2} + \frac{\pi}{4} \middle| k^2\right) = \mathbf{F}\left(\frac{\theta(\sigma)}{2} + \frac{\pi}{4} \middle| k^2\right). \quad (18)$$

Equation (18) can be inverted by utilizing Jacobi elliptic functions. In particular, the Jacobi amplitude function (see, e.g., [42]) is the inverse of F , i.e.,

$$\mathbf{am}(\mathbf{F}(\phi | k^2) | k^2) = \phi. \quad (19)$$

From now on we will drop the k^2 from the arguments and write $\mathbf{am}(\phi)$ for $\mathbf{am}(\phi | k^2)$ and $\mathbf{F}(\phi)$ for $\mathbf{F}(\phi | k^2)$, unless a different parameter is used. Using (19), (18) can be inverted to obtain the following solution:

$$\theta(\sigma) = 2 \mathbf{am}\left(\pm \frac{\omega_\epsilon}{k} \sigma + \mathbf{F}\left(\frac{\pi}{4} + \frac{\theta_0}{2}\right)\right) - \frac{\pi}{2}. \quad (20)$$

Evaluation of the Hamiltonian of (9) at $\sigma = 0$ gives

$$\mathcal{E} = \frac{1}{2}(\theta'_0)^2 + \omega_\epsilon^2 \sin \theta_0, \quad (21)$$

where $\theta'_0 = d\theta(0)/d\sigma$. Using (11) and (21) we see that (20) gives $\theta(\sigma, \theta_0, \theta'_0, \omega_\epsilon)$, as expected for the solution of the initial value problem. To solve the boundary value problem where $\theta'_1 = 0$, we use the identity $d \mathbf{am}(u)/du = \mathbf{dn}(u)$ and hence

$$\frac{d\theta(\sigma)}{d\sigma} = \pm 2 \frac{\omega_\epsilon}{k} \mathbf{dn}\left(\pm \frac{\omega_\epsilon}{k} \sigma + \mathbf{F}\left(\frac{\pi}{4} + \frac{\theta_0}{2}\right)\right), \quad (22)$$

and therefore the boundary condition gives

$$\theta'_1 = \pm 2 \frac{\omega_\epsilon}{k} \mathbf{dn}\left(\pm \frac{\omega_\epsilon}{k} + \mathbf{F}\left(\frac{\pi}{4} + \frac{\theta_0}{2}\right)\right) = 0. \quad (23)$$

Because elliptic integrals and functions usually consider the range $0 \leq k^2 \leq 1$, while we have (13), we use the identity

$$\mathbf{dn}(u | k^2) = \mathbf{cn}(ku | k^{-2}) \quad (24)$$

to write the boundary condition of (23) in the form

$$\mathbf{cn}\left(\pm \omega_\epsilon + k \mathbf{F}\left(\frac{\pi}{4} + \frac{\theta_0}{2} \middle| k^2\right)\right) \Big|_{k^{-2}} = 0. \quad (25)$$

Equation (25) gives a condition relating θ'_0 to ω_ϵ for fixed θ_0 . Because of the periodic nature of $\mathbf{cn}(u)$, these are quantized according to

$$\pm \omega_\epsilon + k \mathbf{F}\left(\frac{\pi}{4} + \frac{\theta_0}{2} \middle| k^2\right) = (2n + 1)\mathbf{K}(k^{-2}), \quad n \in \mathbb{Z}, \quad (26)$$

where $\mathbf{K}(k^{-2}) = \mathbf{F}(\pi/2 | k^{-2})$.

To summarize, we collect all our parameters together,

$$k^2 = \frac{2}{1 + \xi}, \quad \xi = \frac{\mathcal{E}}{\omega_\epsilon^2}, \quad \mathcal{E} = \frac{1}{2}(\theta'_0)^2 + \omega_\epsilon^2 \sin \theta_0.$$

Note that for fixed and given ω_ϵ and θ_0 , the above analysis tells us what θ'_0 must be to hit our boundary condition $\theta'_1 = 0$.

So far we have followed a conventional and straightforward path leading to the solution of (20). Except for the shift in phase and the boundary value nature of this solution, it is standard for a one-degree-of-freedom Hamiltonian system: it depends on two parameters related to possible initial

conditions θ_0 and θ'_0 via \mathcal{E} and one parameter ω_ϵ , which we have treated as a given constant. We proceed now by examining in general terms the boundary value nature of our problem with the imposition of the self-consistency constraint of (5).

Consider a general system of differential equations of the form

$$\frac{d^2\theta}{d\sigma^2} = f(\theta, \lambda), \quad (27)$$

where λ is a parameter. Often one uses a shooting method to solve the boundary value problems for equations of this type, i.e., a sequence of initial conditions are integrated numerically for choices of the parameter λ until the desired boundary condition is reached. This procedure usually selects out discrete values for λ , which for linear systems would be eigenvalues. However, if one has an analytical solution to the initial value problem, as we do, this can be used to relate initial and final values. A condition that relates derivatives at the end points, here taken to be $\sigma = 0$ and 1, follows immediately upon integrating (27), i.e.,

$$\theta'_1 - \theta'_0 = \int_0^1 f(\theta, \lambda) d\sigma. \quad (28)$$

Self-consistency means that the parameter λ depends functionally on the solution $\theta(\sigma)$. For our problem at hand, the role played by λ is ω_ϵ , and this self-consistency requires the solution of (20) be consistent with the ω_ϵ as calculated from (5) with the insertion of (20). As a first step toward imposing this self-consistency constraint, analogous to (28), we integrate (3) to obtain an expression for the height of the hair in terms of an initial condition, viz.,

$$\theta'_0 = \omega_\epsilon^2 \int_0^1 \cos \theta(\sigma) d\sigma = \omega^2 \frac{h_1}{1 - \epsilon h_1} = \frac{1}{\epsilon} (\omega_\epsilon^2 - \omega^2), \quad (29)$$

where $\theta'_0 = d\theta(0)/d\sigma$, and h_1 is the dimensionless height of the hair, the dimensional height being $h_1 L$. The last equality of (29) follows upon eliminating h_1 using (5). The hair problem is complicated because the quantity ω_ϵ^2 depends on the solution of the boundary value problem (5) to give (29). Fortuitously, this quantity only depends on h_1 . For general problems of this nature of the form of (28), these two quantities would not in general depend on a single parameter like this.

Evidently, we must calculate h_1 . In fact, we can explicitly calculate $h(\sigma)$, the height of the hair at parameter value σ (see the Appendix),

$$\begin{aligned} h(\sigma) &= \int_0^\sigma \cos \theta(\sigma') d\sigma' \\ &= \frac{2}{k\omega_\epsilon} \left[\sqrt{1 - k^2 \sin^2(\pi/4 + \theta_0/2)} - \mathbf{dn} \left(\pm \frac{\omega_\epsilon}{k} \sigma + \mathbf{F}(\pi/4 + \theta_0/2) \right) \right]. \end{aligned} \quad (30)$$

Next, we write ω_ϵ in terms of ω and ϵ by inserting the last equality of (29) into (21), giving

$$\omega_\epsilon^2 \mp \epsilon \sqrt{2\mathcal{E} - 2\omega_\epsilon^2 \sin \theta_0} = \omega^2. \quad (31)$$

Thus the self-consistent solution of our boundary value problem is fully determined by the following:

$$\theta(\sigma; \theta_0, \epsilon, \omega) = 2 \mathbf{am} \left(\pm \omega_\epsilon \sqrt{\frac{\xi + 1}{2}} \sigma + \mathbf{F} \left(\frac{\pi}{4} + \frac{\theta_0}{2} \middle| k^2 \right) \middle| k^2 \right) - \frac{\pi}{2}, \quad (32)$$

where $0 \leq \sigma \leq 1$ is our dimensionless parameter and

$$0 = \pm \omega_\epsilon + k \mathbf{F} \left(\frac{\pi}{4} + \frac{\theta_0}{2} \middle| k^2 \right) - (2n + 1) \mathbf{K}(k^{-2}), \quad (33)$$

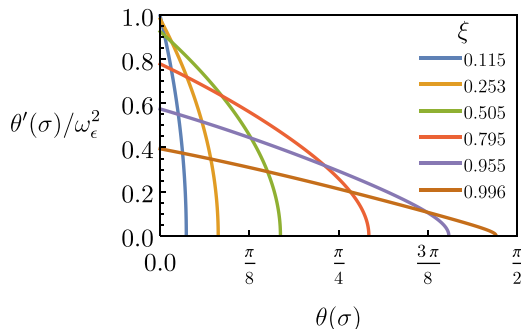


FIG. 3. Phase portraits for a selected set of $0 \leq \xi \leq 1$, a scaled measure of the energy, and their corresponding profiles. $\xi = 1$ corresponds to the separatrix. Trajectories start at $\theta(0) = 0$ and end at $\theta'(1) = 0$.

$$\omega_\epsilon^2 = \omega^2 \pm \epsilon \omega_\epsilon \sqrt{2\xi - 2 \sin \theta_0}, \quad (34)$$

$$k^2 = \frac{2}{\xi + 1}. \quad (35)$$

Note, $k\mathbf{F}(\varphi | k^2) = \mathbf{F}(\bar{\varphi} | k^{-2})$, where $\sin \bar{\varphi} = k \sin \varphi$ [see Eq. (8.127) of [43]], can be used when evaluating (33). Here (33) with (35) determines ω_ϵ as a function of θ_0 and ξ , which with (34) determines ξ as a function of θ_0 , ϵ , and ω . We note in passing that the variable ξ is related to the physically perspicuous variable h_1 according to

$$\xi = \frac{\omega^2}{2} \frac{h_1}{(1 - \epsilon h_1)^2} + \sin \theta_0.$$

In Sec. IV we will evaluate (32) for various cases. We will see that for physically realizable solutions of interest, we must set $n = 0$ in (33) and select the $+$ branch. In practice, we use root finding to solve (33) and (34).

IV. PHASE SPACE INTERPRETATION

Because (3) is isomorphic to the differential equation for a pendulum, it is helpful to interpret our analytical solutions in terms of motion in the pendulum phase space. In this section we do this, first for hairs with $\theta_0 = 0$ and then for $\theta_0 \neq 0$.

A. Vertical hairs: $\theta_0 = 0$

Figure 3 shows several different trajectories, corresponding to different values of ξ , for the case in which $\theta_0 = 0$. Here, only the solutions that stop when they intersect $\theta'_1 = 0$ once are shown, but we do observe other solutions corresponding to trajectories completing one or several orbits, especially at higher values of ξ .

Observe, $\xi = \mathcal{E}/\omega_\epsilon^2$ and \mathcal{E} are both measures of the system's energy (Hamiltonian) since they only differ by a proportionality constant once self-consistency is enforced. We prefer to use ξ in the following figures and analysis because $-1 \leq \xi \leq 1$, while \mathcal{E} is unbounded. In addition, our analytic solution is written more concisely in terms of ξ . Figure 3 shows the phase space with energy surfaces parametrized by ξ . Note, because ξ is used and because the ordinate is $\theta'/\omega_\epsilon^2$, the energy surfaces are not nested as usual. In Fig. 3, as $\xi \rightarrow 1$ the orbit approaches the separatrix and $\xi = 0$ corresponds to the undeformed hair where $\theta(\sigma) \equiv 0$.

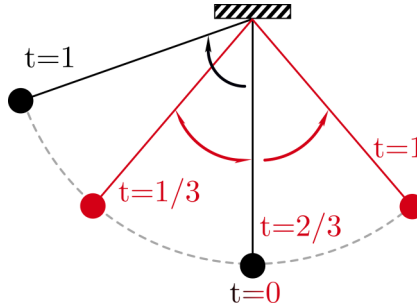


FIG. 4. The problem of a cantilevered hair with a point load at its end is isomorphic to the equation of motion for a pendulum with the initial conditions $\theta(t = 0) = 0$ and $\dot{\theta}(t = 1) = 0$. Because multiple different orbits can satisfy these conditions for a given choice in parameters (e.g., the blue and black orbits of the figure), both the cantilevered hair and the pendulum problem posed above are not unique.

Within the pendulum analogy, ω_ϵ acts as a natural frequency. The boundary conditions $\theta_0 = 0$ and $\theta'_1 = 0$ describe a pendulum trajectory starting at $\theta = 0$ and ending when $\dot{\theta} = 0$ in a time T . The largest possible initial velocity that satisfies these conditions corresponds to a phase-space trajectory entirely confined to the first quadrant. At a threshold natural frequency, other starting velocities can also satisfy the “initial” conditions, but they must correspond to orbits that exit the first quadrant.

Figure 4 depicts two orbits for a given choice of parameters. The first (black) starts at $\theta_0 = 0$ with some $\dot{\theta}_0 \neq 0$ and the trajectory evolves until $\dot{\theta}_1 = 0$. On the other hand, the red orbit reaches its first maximum when $\dot{\theta}(t = 1/3) = 0$ and it oscillates in the other direction until finally reaching $\dot{\theta}_1 = 0$. When not equal to zero, the branch index n [shown in Eq. (32)] selects out these lower period orbits. In addition to these two solutions in our example above, there are two more with an opposite sign in $\dot{\theta}_0$. This choice in direction is reflected by the \pm sign in our solution. Lastly, note that for the sake of clarity, we have drawn Fig. 4 without the $\pi/2$ angle shift that is present, but the principles discussed in this paragraph are unchanged when accounting for this shift (the orbits of interest remain bounded whether or not there is an angle shift).

For the hairs, choices of $n \neq 0$ and/or negative curvature branches correspond to “twirling” profiles (see Fig. 5). These orbits are not physically realizable for simple shear flow experiments for either of two reasons:

(i) Hair profiles intersect the surface they are mounted on (or also themselves). This is possible because the model does not consider hair-surface interactions.

(ii) The assumption that shear stress is concentrated at the hair-tip breaks down because the hair-tip is no longer the portion exposed to shear flow.

These solutions are an important consideration nevertheless because numerical algorithms can be susceptible to converging to them.

All accessible solutions for a discrete list of ϵ values and a range of ω^2 are plotted in Fig. 5. In panel (a) we plot the energy \mathcal{E} (a measure of θ'_0) versus ω^2 for the values of ϵ color-coded in panel (c). The blue curve corresponds to $\epsilon = 0$, the case in which self-consistency vanishes, while the orange curve shows the distortion caused as ϵ approaches unity. This plot makes it clear that the pendulum analogy alone is insufficient to capture predictions of the basic model. Panel (b) shows that the solutions of the self-consistent boundary value problem are completely collapsed when the similarity variable ξ is used instead of \mathcal{E} . In this plot of ξ versus ω_ϵ^2 there is only a single curve. The black lines in this plot depict representative hair profiles: for small ω_ϵ^2 the hair bends only slightly while there is a scaling change for $\omega_\epsilon^2 \gtrsim 1$ as the hair bends significantly. In addition, for larger ω_ϵ^2 we obtain the twirling profiles where the solid and dashed lines of panel (b) indicate positive and negative base curvature, respectively. Panel (c) shows that the physically realizable branch can be partially collapsed by plotting ξ versus $\omega^2/(1 - \epsilon)$. In the case of the physically realizable solutions,

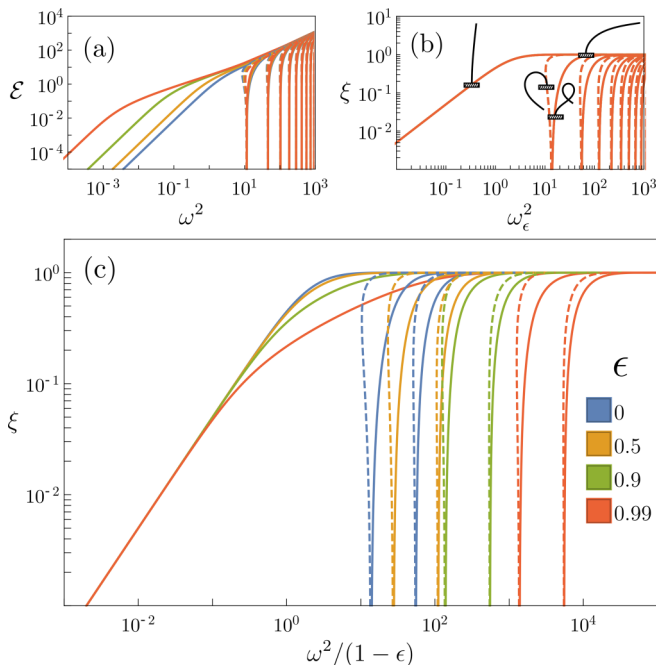


FIG. 5. Plots of solutions of the boundary value problem posed in Sec. II for the case $\theta_0 = 0$ depending on the two parameters, ω^2 and ϵ . (a) Uncollapsed dependence of the energy (Hamiltonian) \mathcal{E} on the two input parameters. (b) Fully collapsed solution space in terms of the similarity variables $\xi = \mathcal{E}/\omega_\epsilon^2$ vs ω_ϵ^2 , with representative hair profiles. Here, solid and dashed lines indicate positive and negative base curvature, respectively. Note, ω_ϵ^2 is a quantity that depends transcendently on ω^2 and ϵ . For weak and strong forcing, we see the predicted scalings of $\xi \approx \omega_\epsilon^2/2$ and $\xi \rightarrow 1$, respectively, with the crossover occurring near $\omega_\epsilon^2/2 \approx 1$. (c) Partial collapse of the solution space is seen using the abscissa $\omega^2/(1-\epsilon)$, showing physically realizable branches with an explicit function of the input parameters. To avoid clutter, only the first three branches (and their negative curvature counterparts) are plotted in this panel.

the dependence on ϵ is most apparent for small forcing where the hair height is maximal. For this case (e.g., small imposed fluid velocity $v \ll 1$), $h_1 \rightarrow 1$, i.e., the hair is nearly vertical with $\theta \approx 0$. Thus from (29), $\theta'_0 \approx \omega_\epsilon^2$, which with (21) gives

$$\xi = \frac{\theta'^2}{2\omega_\epsilon^2} + \sin \theta \approx \frac{\theta'^2}{2\omega_\epsilon^2} \approx \frac{\omega_\epsilon^2}{2}. \quad (36)$$

This explains the linear dependence and slope observed in panel (b) of Fig. 5 for small ω_ϵ^2 . For large forcing where $\omega^2 \rightarrow \infty$, the height of the hair asymptotically approaches zero, i.e., $\theta_1 \approx \pi/2$ and $\xi \approx \sin \theta_1 \approx 1$, which explains the asymptote of panel (b) of Fig. 5. In this limit, $\omega_\epsilon^2 \rightarrow \omega^2$ and the ϵ -dependence vanishes. Finally, one expects the crossover between weak and strong forcing behavior to occur near $\omega_\epsilon^2/2 \approx 1$, and indeed this is the case.

The self-consistency condition captures the fact that hairs deform to reduce drag. This effect is controlled by the hair length to channel height ratio, ϵ . Figure 5(a) reveals that increasing ϵ corresponds to an increase in the system's Hamiltonian, \mathcal{E} . Through rearrangement of Eq. (31) to $\omega_\epsilon^2 = \omega^2 + \epsilon\sqrt{2\mathcal{E}}$ (here, the physically realizable branch has been selected), we see that as ϵ grows, the forcing parameter ω_ϵ^2 must also increase.

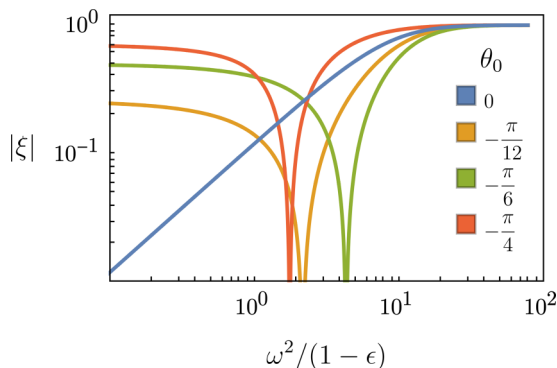


FIG. 6. ξ vs ω_ϵ plotted using Eq. (32) for different values of θ_0 . Hairs with a negative base-angle have negative energy at low ω , and transition to positive energy as ω increases. Figure created with $\epsilon = 0.61$.

B. Angled hairs: $\theta_0 \neq 0$

Next, we plot ξ versus ω_ϵ for different values of θ_0 in Fig. 6. For negative θ_0 , shear flow is against the grain. As the forcing increases, hairs reorient to align with the fluid velocity until $\theta_1 = 0$, which corresponds to $\xi = 0$. Further increasing the forcing parameter brings the system into the flow alignment regime, scaling the same for all θ_0 .

On the other hand, increasing θ_0 results in flow with the grain. Flow alignment can be achieved with a smaller forcing parameter (compared to $\theta_0 = 0$), and the dependence of ξ on $\omega^2/(1 - \epsilon)$ approaches a horizontal line.

V. HAIR PROFILES, DISCUSSION, AND COMPARISONS

Recall from Sec. II, the unit tangent is given by $\mathbf{R}' = \hat{\mathbf{T}}$, which implies $x'(\sigma) = \sin \theta(\sigma)$ and $z'(\sigma) = \cos \theta(\sigma)$. Thus, given our solutions of Sec. III for $\theta(\sigma)$, we can plot z versus x for the hair profiles. In this section, we compare hair profiles obtained by our analytic solutions with those obtained by direct numerical integration. A standard numerical method for nonlinear boundary value problems is to use a shooting code, whereby initial values are incremented until the desired boundary value is obtained. In [32] such a shooting code with a standard ordinary differential equation algorithm was used to integrate the pendulum equations of (2), with an adaptation allowing for the θ -dependence in ω_ϵ . Another approach is to make a central difference approximation to the second derivative of (2), representing θ along the centerline of the hair by a mesh of N segments with values θ_i ($i = 1, 2, \dots, N$). This gives a sequence of algebraic equations with the boundary conditions built into the first and last equation. Coupling of the equations is provided by both the differencing and the self-consistency through ω_ϵ . An example of this procedure is given in [44], where the more complicated problem of a filament subject to three-dimensional dynamical behavior is solved by discretizing in both space and time. Associated with this method is a root finding problem, which for the time-independent case involves solving N equations for each mesh value θ_i . Because there is not a concise description of how each of θ_i asymptotically scales with the forcing parameter, ω , convergence to physical solutions is not always guaranteed.

In Fig. 7 a set of profiles is shown, comparing our analytic solution with numerical solutions obtained by using the mesh discretization described above. At low forcing, both approaches converge to the same physical solution. At high forcing when the hair becomes more streamlined, the numerical solution fails to converge accurately. The reason for this discrepancy is currently unknown. As shown in Fig. 8(a), increasing the mesh segment number further does not significantly reduce the error in hair height. In Fig. 8(b), we see that error is most concentrated towards the base of the hair for strongly deformed configurations.

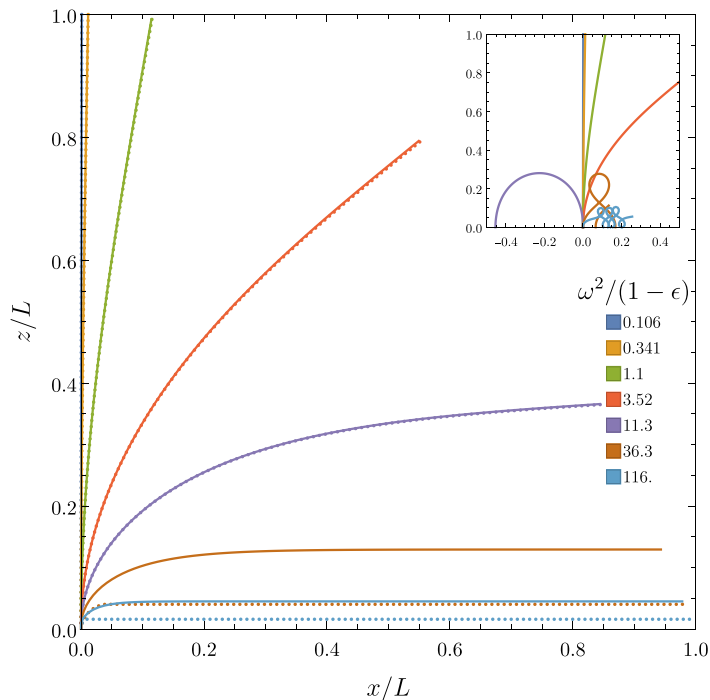


FIG. 7. Comparison of numerical and analytic solutions for a variety of \mathcal{E} . Solid and dashed curves indicate numerical and analytic solutions, respectively. A discretization method was used for the numerical routine with an initial estimate of $\theta_i = 0$ for the outer figure and $\theta_i = -0.1$ for the inset.

Even though there is a root finding problem associated with our analytic solution, it is a single equation (compared to N for the numerical approach). Because of this, and the fact that we know how \mathcal{E} scales in both deformed and undeformed regimes, our analytic method is both simpler to implement and faster to compute than numerical approaches.

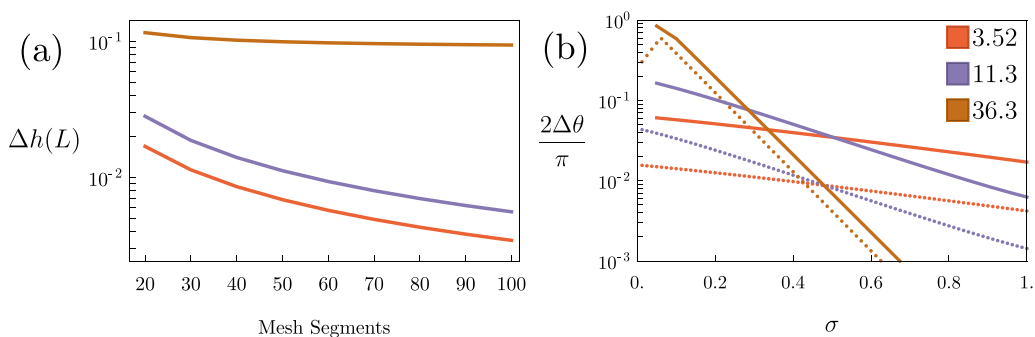


FIG. 8. Convergence of the finite-difference approach to the analytical solution, where $\Delta\theta \equiv \theta_{\text{analytic}} - \theta_{\text{numeric}}$, $\Delta h(L) \equiv h_{\text{analytic}}(L) - h_{\text{numeric}}(L)$, and legend labels correspond to the value of $\omega^2/(1-\epsilon)$. In panel (b), solid and dashed lines are solutions with $N = 20$ and 80 mesh segments, respectively. Error due to the discretized nature of the numerics is most apparent at the base of the hair (i.e., small σ), dropping off as the curvature decreases towards the hair-tip. Increasing mesh segment number has a marginal effect on improving convergence.

We have observed that the analytic solution is about two orders of magnitude faster (0.005 versus 0.5 s for a finite-difference simulation with a mesh size of 80) than the numerical procedure. There is not much difference in obtaining a single solution using either approach in terms of speed. However, problems that involve solving (3) iteratively can benefit significantly from the analytic approach. For example, optimization of the system's rectification properties and solving weakly time-dependent problems [$\omega_\epsilon \rightarrow \omega_\epsilon(t)$] are potentially computationally expensive tasks.

Given a shear stress, what are the profiles of a bed of hairs, which can be dense yet noninteracting? Our solution presented in (32) provides an answer to this question. The inverse problem, where the profiles are used to infer the shear stress, is utilized in a recently developed imaging technique. In [45,46], a bed of flexible micropillars is used to detect near-wall shear stress and velocity fields in turbulent flow. The pillars act as waveguides allowing the tip deflection to be measured when illuminated from below. Our analytic method could be used to derive simple expressions for tip-deflection, which can be utilized in the linear, low deformation regime. Greater flow-detection sensitivity can be achieved by increasing the flexibility of the pillars and operating them in the nonlinear regime [46].

Lastly, we argue that our analytic solution can be used as a basis for understanding problems where the fluid flow has a slow time dependence. In this regime, a hair cycles through its steady-state profiles, and fluid flows within the hair bed can be neglected.

VI. SUMMARY

In this work, we obtained a solution to a differential equation describing the profile of a hair bed immersed in shear flow. This problem differs from previous treatments of cantilevered rods in that the forcing parameter has a functional dependence on the dependent variable, $\theta(\sigma)$. This aspect of the model captures the fact that hairs deform to reduce the fluid induced drag. As interesting as they are, many of these solutions are not physically realizable, and an advantage of our analytic work is that we can select the desired branch. To contrast this, shooting codes and other numerical approaches cannot be guaranteed to converge to this class of solution.

We then compare the analytic solution to a central difference based numerical scheme that performs reasonably well for the range of loading tested, but we can encounter a convergence issue when the curvature at the base is large.

Future work could explore an adiabatic extension of this model to describe time-dependent channel flows.

ACKNOWLEDGMENTS

P.J.M. was supported by U.S. Department of Energy under Contract No. DE-FG05-80ET-53088. J.S. and Z.M.V. contributed equally to this work.

APPENDIX: CALCULATION OF $h(\sigma)$

We wish to calculate $h(\sigma)$ of (30). To this end, let

$$\theta(\sigma) = 2[\mathbf{am}(u) - \pi/4] \quad \text{with} \quad u := \frac{\omega_\epsilon}{k} \sigma + \mathbf{F}\left(\frac{\pi}{4} + \frac{\theta_0}{2}\right). \quad (\text{A1})$$

Using elementary trigonometry identities, we obtain

$$\cos \theta(\sigma) = \cos[2(\mathbf{am}(u) - \pi/4)] = 1 - 2 \sin^2[\mathbf{am}(u) - \pi/4], \quad (\text{A2})$$

$$\sin(\mathbf{am}(u) - \pi/4) = \frac{\sqrt{2}}{2}(\mathbf{sn}(u) - \mathbf{cn}(u)), \quad (\text{A3})$$

with the identities $\mathbf{sn}(u) = \sin(\mathbf{am}(u))$ and $\mathbf{cn}(u) = \cos(\mathbf{am}(u))$. Thus,

$$2 \sin^2(\mathbf{am}(u) - \pi/4) = (\mathbf{sn}(u) - \mathbf{cn}(u))^2 = 1 - 2\mathbf{cn}(u)\mathbf{sn}(u), \quad (\text{A4})$$

using $\mathbf{sn}^2(u) + \mathbf{cn}^2(u) = 1$. So $1 - 2 \sin^2(u) = 2\mathbf{cn}(u)\mathbf{sn}(u)$, from which, with

$$\mathbf{cn}(u)\mathbf{sn}(u) = -\frac{1}{k^2} \frac{d}{du} \mathbf{dn}(u), \quad (\text{A5})$$

we obtain

$$\int_0^\sigma \cos \theta(\sigma') d\sigma' = -\frac{k}{\omega_\epsilon} \frac{2}{k^2} \int_{u_0}^u \frac{d}{du'} \mathbf{dn}(u') du' = \frac{2}{k\omega_\epsilon} (\mathbf{dn}(u_0) - \mathbf{dn}(u)) \quad (\text{A6})$$

using $d\sigma = k du/\omega_\epsilon$, where $u_0 = \mathbf{F}(\pi/4 + \theta_0/2)$. Finally, we use

$$\mathbf{dn}(\mathbf{F}(\phi | k^2)) = \sqrt{1 - k^2 \sin^2 \phi} \quad (\text{A7})$$

to obtain the result of (30).

- [1] K. Autumn, M. Sitti, Y. A. Liang, A. M. Peattie, W. R. Hansen, S. Sponberg, T. W. Kenny, R. Fearing, J. N. Israelachvili, and R. J. Full, Evidence for van der Waals adhesion in gecko setae, *Proc. Natl. Acad. Sci. (USA)* **99**, 12252 (2002).
- [2] B. Cummins, T. Gedeon, I. Klapper, and R. Cortez, Interaction between arthropod filiform hairs in a fluid environment, *J. Theor. Biol.* **247**, 266 (2007).
- [3] C. J. Harper, S. M. Swartz, and E. L. Brainerd, Specialized bat tongue is a hemodynamic nectar mop, *Proc. Natl. Acad. Sci. (USA)* **110**, 8852 (2013).
- [4] N. Reicher and Z. Uni, Intestinal brush border assembly during the peri-hatch period and its contribution to surface area expansion, *Poult. Sci.* **100**, 101401 (2021).
- [5] Y.-N. Zou, D.-J. Zhang, C.-Y. Liu, and Q.-S. Wu, Relationships between mycorrhizae and root hairs, *Pak. J. Bot.* **51**, 727 (2019).
- [6] M. Luhar and H. M. Nepf, Flow-induced reconfiguration of buoyant and flexible aquatic vegetation, *Limnol. Oceanogr.* **56**, 2003 (2011).
- [7] S. Weinbaum, L. M. Cancel, B. M. Fu, and J. M. Tarbell, The Glycocalyx and its role in vascular physiology and vascular related diseases, *Cardiovasc. Eng. Technol.* **12**, 37 (2021).
- [8] S. Chateau, J. Favier, S. Poncet, and U. D'Ortona, Why antiplectic metachronal cilia waves are optimal to transport bronchial mucus, *Phys. Rev. E* **100**, 042405 (2019).
- [9] H. Angleys and L. Østergaard, Krogh's capillary recruitment hypothesis, 100 years on: Is the opening of previously closed capillaries necessary to ensure muscle oxygenation during exercise? *Am. J. Physiol.: Heart Circ. Physiol.* **318**, H425 (2020).
- [10] G. Walker, A. B. Yulf, and J. Ratcliffe, The adhesive organ of the blowfly, *Calliphora vomitoria*: A functional approach (Diptera: Calliphoridae), *J. Zool.* **205**, 297 (1985).
- [11] J. M. R. Bullock and W. Federle, Beetle adhesive hairs differ in stiffness and stickiness: In vivo adhesion measurements on individual setae, *Naturwissenschaften* **98**, 381 (2011).
- [12] R. B. Suter, G. E. Stratton, and P. R. Miller, Taxonomic variation among spiders in the ability to repel water: Surface adhesion and hair density, *J. Arachnology* **32**, 11 (2004).
- [13] W. Kim, T. Gilet, and J. W. M. Bush, Optimal concentrations in nectar feeding, *Proc. Natl. Acad. Sci. (USA)* **108**, 16618 (2011).
- [14] A. Nasto, P.-T. Brun, and A. E. Hosoi, Viscous entrainment on hairy surfaces, *Phys. Rev. Fluids* **3**, 024002 (2018).
- [15] P. Guo, A. M. Weinstein, and S. Weinbaum, A hydrodynamic mechanosensory hypothesis for brush border microvilli, *Am. J. Physiol. – Renal Physiol.* **279**, F698 (2000).

- [16] K. Hood, M. S. Suryateja Jammalamadaka, and A. E. Hosoi, Marine crustaceans with hairy appendages: Role of hydrodynamic boundary layers in sensing and feeding, *Phys. Rev. Fluids* **4**, 114102 (2019).
- [17] J.-B. Thomazo, J. Contreras Pastenes, C. J. Pipe, B. Le Révérend, E. Wandersman, and A. M. Prevost, Probing in-mouth texture perception with a biomimetic tongue, *J. R. Soc. Interface* **16**, 20190362 (2019).
- [18] J.-B. Thomazo, E. Lauga, B. Le Révérend, E. Wandersman, and A. M. Prevost, Collective stiffening of soft hair assemblies, *Phys. Rev. E* **102**, 010602(R) (2020).
- [19] D. Takagi and J. Rudi Strickler, Active hydrodynamic imaging of a rigid spherical particle, *Sci. Rep.* **10**, 2665 (2020).
- [20] B. P. Chagnaud, C. Brücker, M. H. Hofmann, and H. Bleckmann, Measuring flow velocity and flow direction by spatial and temporal analysis of flow fluctuations, *J. Neurosci.* **28**, 4479 (2008).
- [21] O. Dangles, D. Pierre, C. Magal, F. Vannier, and J. Casas, Ontogeny of air-motion sensing in cricket, *J. Exp. Biol.* **209**, 4363 (2006).
- [22] G. P. Sutton, D. Clarke, E. L. Morley, and D. Robert, Mechanosensory hairs in bumblebees (*Bombus terrestris*) detect weak electric fields, *Proc. Natl. Acad. Sci. (USA)* **113**, 7261 (2016).
- [23] O. du Roure, A. Lindner, E. N. Nazockdast, and M. J. Shelley, Dynamics of flexible fibers in viscous flows and fluids, *Annu. Rev. Fluid Mech.* **51**, 539 (2019).
- [24] A. Nasto, M. Regli, P.-T. Brun, J. Alvarado, C. Clanet, and A. E. Hosoi, Air entrainment in hairy surfaces, *Phys. Rev. Fluids* **1**, 033905 (2016).
- [25] S. Hanasoge, M. Ballard, P. J. Hesketh, and A. Alexeev, Asymmetric motion of magnetically actuated artificial cilia, *Lab Chip* **17**, 3138 (2017).
- [26] X. Zhang, J. Guo, X. Fu, D. Zhang, and Y. Zhao, Tailoring flexible arrays for artificial cilia actuators, *Adv. Intell. Syst.* **3**, 2000225 (2021).
- [27] Y. Wang, J. den Toonder, R. Cardinaels, and P. Anderson, A continuous roll-pulling approach for the fabrication of magnetic artificial cilia with microfluidic pumping capability, *Lab Chip* **16**, 2277 (2016).
- [28] J. Paek and J. Kim, Microsphere-assisted fabrication of high aspect-ratio elastomeric micropillars and waveguides, *Nat. Commun.* **5**, 3324 (2014).
- [29] J. S. Wexler, P. H. Trinh, H. Berthet, N. Quennouz, O. du Roure, H. E. Huppert, A. Lindner, and H. A. Stone, Bending of elastic fibres in viscous flows: the influence of confinement, *J. Fluid Mech.* **720**, 517 (2013).
- [30] S. Zhang, Z. Cui, Y. Wang, and J. den Toonder, Metachronal μ -cilia for on-chip integrated pumps and climbing robots, *ACS Appl. Mater. Interfaces* **13**, 20845 (2021).
- [31] E. Milana, R. Zhang, M. R. Vetrano, S. Peerlinck, M. De Volder, P. R. Onck, D. Reynaerts, and B. Gorissen, Metachronal patterns in artificial cilia for low Reynolds number fluid propulsion, *Sci. Adv.* **6**, eabd2508 (2020).
- [32] J. Alvarado, J. Comtet, E. de Langre, and A. E. Hosoi, Nonlinear flow response of soft hair beds, *Nat. Phys.* **13**, 1014 (2017).
- [33] D. B. Stein and M. J. Shelley, Coarse graining the dynamics of immersed and driven fiber assemblies, *Phys. Rev. Fluids* **4**, 073302 (2019).
- [34] E.-S. Shanko, Y. van de Burgt, P. D. Anderson, and J. M. J. den Toonder, Microfluidic magnetic mixing at low Reynolds numbers and in stagnant fluids, *Micromachines* **10**, 731 (2019).
- [35] R. Zhang, J. den Toonder, and P. R. Onck, Transport and mixing by metachronal waves in nonreciprocal soft robotic pneumatic artificial cilia at low Reynolds numbers, *Phys. Fluids* **33**, 092009 (2021).
- [36] A. Saberi, S. Zhang, C. van den Besselaar, H. Kandail, J. M. J. den Toonder, and N. A. Kurniawan, A stirring system using suspended magnetically-actuated pillars for controlled cell clustering, *Soft Matter* **15**, 1435 (2019).
- [37] B. Audoly and Y. Pomeau, *Elasticity and Geometry: From Hair Curls to the Nonlinear Response of Shells*, illustrated ed. (Oxford University Press, Oxford, 2010).
- [38] N. Luminari, Modeling and simulation of flows over and through fibrous porous media, Ph.D. thesis, Université de Toulouse, 2018.
- [39] L. Petrovic, M. Henne, and J. Anderson (unpublished).
- [40] D. Ryu (unpublished).

- [41] H. Iben, M. Meyer, L. Petrovic, O. Soares, J. Anderson, and A. Witkin, Artistic simulation of curly hair, in *Proceedings of the 12th ACM SIGGRAPH/Eurographics Symposium on Computer Animation–SCA '13* (ACM, New York, 2013), p. 63.
- [42] *Handbook of Mathematical Functions: with Formulas, Graphs, and Mathematical Tables*, edited by M. Abramowitz and I. A. Stegun (Dover, New York, 1965).
- [43] I. S. Gradshteyn and I. M. Ryzhik, *Table of Integrals, Series, and Products*, 7th ed. (Elsevier/Academic, Amsterdam, 2007).
- [44] M. Gazzola, L. H. Dudte, A. G. McCormick, and L. Mahadevan, Forward and inverse problems in the mechanics of soft filaments, [R. Soc. Open Sci. 5, 171628 \(2018\)](#).
- [45] Y. Liu, M. Klaas, and W. Schröder, Measurements of the wall-shear stress distribution in turbulent channel flow using the micro-pillar shear stress sensor MPS3, [Exp. Therm. Fluid Sci. 106, 171 \(2019\)](#).
- [46] C. Brücker, Evidence of rare backflow and skin-friction critical points in near-wall turbulence using micropillar imaging, [Phys. Fluids 27, 031705 \(2015\)](#).